Feitian Zhang[1]
Smart Microsystems Lab,
Department of Electrical
and Computer Engineering,
Michigan State University,
East Lansing, MI 48823
e-mail: zhangzft@gmail.com

Fumin Zhang
School of Electrical and Computer Engineering,
Georgia Institute of Technology,
Atlanta, GA 30332
e-mail: fumin@gatech.edu

Xiaobo Tan
Smart Microsystems Lab,
Department of Electrical
and Computer Engineering,
Michigan State University,
East Lansing, MI 48823
e-mail: xbtan@msu.edu

Tail-Enabled Spiraling Maneuver for Gliding Robotic Fish

Gliding robotic fish, a new type of underwater robot, combines both strengths of underwater gliders and robotic fish, featuring long operation duration and high maneuverability. In this paper, we present both analytical and experimental results on a novel gliding motion, tail-enabled three-dimensional (3D) spiraling, which is well suited for sampling a water column. A dynamic model of a gliding robotic fish with a deflected tail is first established. The equations for the relative equilibria corresponding to steady-state spiraling are derived and then solved recursively using Newton's method. The region of convergence for Newton's method is examined numerically. We then establish the local asymptotic stability of the computed equilibria through Jacobian analysis and further numerically explore the basins of attraction. Experiments have been conducted on a fish-shaped miniature underwater glider with a deflected tail, where a gliding-induced 3D spiraling maneuver is confirmed. Furthermore, consistent with model predictions, experimental results have shown that the achievable turning radius of the spiraling can be as small as less than 0.4 m, demonstrating the high maneuverability. [DOI: 10.1115/1.4026965]

1 Introduction

Aquatic environmental sampling is a key challenge worldwide in securing sustainable water resources. Autonomous underwater robots hold the potential in this domain for monitoring water quality, tracking oil spills, and patrolling seaports, to name a few. High energy-efficiency and high maneuverability are desired characteristics for such robots in order to operate in versatile environments such as lakes, rivers, and the ocean. Underwater gliders, which propel themselves by changing the net buoyancy and the center of gravity, have demonstrated low power consumption and long operating duration. Examples of commercial underwater gliders include the Seaglider [1], Spray [2], and Slocum [3]. These gliders are designed for ocean sampling purposes with typical length of 1–2 m and weight of 50 kg or more. It is generally not energy efficient for underwater gliders to operate in environments such as rivers and shallow lakes. Furthermore, the maneuverability of gliders is typically poor. A different class of aquatic robots that mimics fish motion has received great attention over the past two decades. These robots, often called robotic fish, can swim by deforming the body and fish-like appendages [4–17]. Like their biological counterparts, robotic fish are highly maneuverable in a broad range of environments. However, they require constant actuation for locomotion and maneuvering and cannot operate for extended periods of time without battery recharge.

An intriguing design concept is to combine attractive features of underwater gliders and robotic fish [18] to offer maneuverability and endurance at the same time. Termed *gliding robotic fish*, such a robot would achieve locomotion mostly through adjusting its net buoyancy and center of mass, like an underwater glider. On the other hand, steering is mostly realized by actively controlled fins, similar to a robotic fish. In addition, gliding robotic fish can be designed to have much smaller size than a commercial underwater glider and operate in shallow water for an extended period of time.

The typical operation of underwater gliders is rectilinear, zigzag gliding in a vertical plane, while the nominal operation of robotic fish is fin-flapping-enabled swimming. There are also a few studies about the three-dimensional (3D) spiral gliding of underwater gliders, which is predominantly realized by translating or rotating an internal mass [19–24]. In this paper, we investigate a novel form of gliding where a deflected tail induces 3D spiraling motion [25], which enables energy-efficient maneuvering without constant actuation of the tail. Throughout the paper, the term "spiral" refers to a 3D helical motion and, in most part, to a helical motion with constant radius under a given set of (fixed) inputs. On the application side, the spiraling motion carries significant relevance to water column sampling. A water column is a conceptual narrow volume (like a narrow cylinder) of water stretching vertically from the surface to the bottom. Water column sampling is a routine surveying method in environmental studies for evaluating the stratification or mixing of water layers and for monitoring the distributions of physical and biological processes [26]. Existing approaches for water column sampling typically involve lowering and raising sensors off a boat or ship, which are time consuming and costly. The spiraling motion produced by underwater gliders has a typical turning radius on the order of 30–50 m, not suitable for the water-column sampling tasks in lakes and shallow waters where higher spatial resolution is needed. In this paper, we will show that with tail-deflected gliding, a gliding robotic fish can achieve a spiraling radius as small as less than 0.4 m, showing great potential for sampling water columns in versatile environments.

The dynamics of underwater gliders have been studied mostly for movable mass and net buoyancy-controlled gliding in the literature [19–24,27,28]. In this paper, we focus on the influence of a deflected tail and study the resulting 3D spiraling motion. For path planning and control, it is important to know the parameters characterizing the spiral under a given set of control inputs. For this purpose, based on the dynamic model, we derive the equations for the relative equilibria corresponding to steady-state spiraling. These equations are highly nonlinear and cannot be solved analytically. We introduce Newton's method to obtain the equilibria recursively and investigate the impacts of various control inputs (net buoyancy, movable mass location, and tail deflection angle) on the spiraling parameters, such as the turning radius and vertical speed. We also numerically explore the region of convergence for the algorithm to gain insight into the proper choice of

[1]Corresponding author.

Contributed by the Dynamic Systems Division of ASME for publication in the Journal of Dynamic Systems, Measurement, and Control. Manuscript received May 5, 2013; final manuscript received February 20, 2014; published online May 8, 2014. Assoc. Editor: Alexander Leonessa.

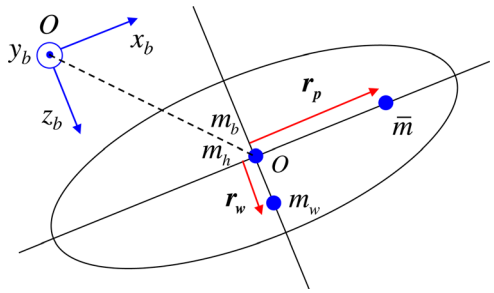

Fig. 1 The mass distribution of the gliding robotic fish (side view)

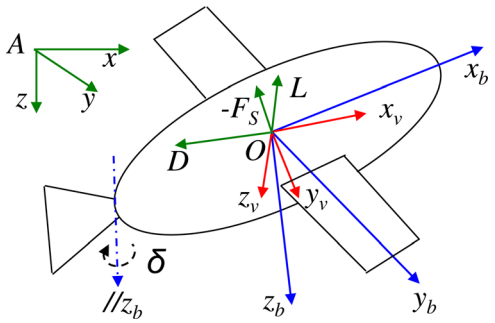

Fig. 2 Illustration of the reference frames and hydrodynamic forces

initial conditions. For the computed relative equilibria, we show that they are locally asymptotically stable through Jacobian analysis. Through simulation of the dynamic model, we further explore the basins of attraction for the equilibria and the convergence speeds from different initial conditions, which seems to suggest that the equilibria are asymptotically stable with large basins of attraction. Finally, we have performed experiments on a fish-shaped miniature underwater glider [29] with a swappable tail to confirm the spiral motion and validate the derived model.

The remainder of the paper is organized as follows. In Sec. 2, we present the full dynamic model of the gliding robotic fish incorporating the influence of a deflectable tail. The steady-state spiraling motion is characterized in Sec. 3. In particular, six nonlinear equations corresponding to the relative equilibria are derived in Sec. 3.1 and then solved with Newton's method in Sec. 3.2. The region of convergence for the algorithm is discussed in Sec. 3.3. Local stability analysis is conducted using linearization in Sec. 3.4, while the analysis of the basins of attraction is presented in Sec. 3.5. Experimental results are presented in Sec. 4. Concluding remarks are provided in Sec. 5.

2 Dynamic Modeling of Gliding With a Deflected Tail

2.1 Full Dynamic Model. A gliding robotic fish is a combination of a miniature underwater glider and a robotic fish, and its modeling will need to incorporate the effects of both. For the spiraling motion, the tail is not constantly flapping and we treat it as a control surface and a source for external forces and moments. The robot is modeled as a rigid-body system, including an internal movable mass for center-of-mass control and a water tank for buoyancy adjustment [27,29]. On the other hand, the deflected tail provides external thrust force and side force as well as the yaw moment.

Figure 1 shows the mass distribution within the robot. The stationary body mass m_s (excluding the movable mass) has three components: hull mass m_h (assumed to be uniformly distributed), point mass m_w accounting for nonuniform hull mass distribution with displacement $\boldsymbol{r_w}$ with respect to the geometry center (GC), and ballast mass m_b (water in the tank) at the GC, which is a reasonable simplification since the effect on the center of gravity caused by the water in the tank is negligible compared with the effect from the movable mass. The movable mass $\bar{m}$, which is located at $\boldsymbol{r_p}$ with respect to the GC, provides a moment to the robot. The motion of the movable mass is restricted to the longitudinal axis. The robot hull displaces a volume of fluid of mass m. Let $m_0 = m_s + \bar{m} - m$ represents the excess mass (negative net buoyancy). The robot will sink if $m_0 > 0$ and ascend if $m_0 < 0$.

The relevant coordinate reference frames are defined following the standard convention. The body-fixed reference frame, denoted as $Ox_by_bz_b$ and shown in Fig. 2, has its origin O at the geometry center, so the origin will be the point of application for the buoyancy force. The Ox_b axis is along the body's longitudinal axis pointing to the head; the Oz_b axis is perpendicular to Ox_b axis in the sagittal plane of the robot pointing downward, and Oy_b axis is automatically formed by the right-hand orthonormal principle. In the inertial frame $Axyz$, Az axis is along gravity direction, and Ax/Ay are defined in the horizontal plane, while the origin A is a fixed point in space.

As commonly used in the literature, $\boldsymbol{R}$ represents the rotation matrix from the body-fixed reference frame to the inertial frame, following the conventional 3-2-1 intrinsic rotation sequence [30]. $\boldsymbol{R}$ is parameterized by three Euler angles: the roll angle ϕ, the pitch angle θ, and the yaw angle ψ. Here

$$\boldsymbol{R} = \begin{pmatrix} \cos\theta\cos\phi & \sin\phi\sin\theta\cos\psi - \cos\phi\sin\psi & \cos\phi\sin\theta\cos\psi + \sin\phi\sin\psi \\ \cos\theta\sin\psi & \cos\phi\cos\psi + \sin\phi\sin\theta\sin\psi & -\sin\phi\cos\psi + \cos\phi\sin\theta\sin\psi \\ -\sin\theta & \sin\phi\cos\theta & \cos\phi\cos\theta \end{pmatrix} \tag{1}$$

Let $\boldsymbol{v_b} = (v_1\, v_2\, v_3)^T$ and $\boldsymbol{\omega_b} = (\omega_1\, \omega_2\, \omega_3)^T$ represent the translational velocity and angular velocity, respectively, expressed in the body-fixed frame. The subscript b indicates that the vector is expressed in the body-fixed frame, and this notation is applied throughout this paper.

We assume that the tail fin is rigid and pivots at the junction between the body and the tail about the Oz_b axis. The tail induces an external thrust force $\boldsymbol{F}_t$ on the robot when it flaps. There are also other hydrodynamic forces and moments generated because of the relative movement between the tail and the surrounding water, like the side force and the yaw moment.

By extending the previous modeling work for underwater gliders [29], we obtain the dynamic model for a gliding robot with a deflected tail fin as the following:

$$\dot{\boldsymbol{v}}_{\boldsymbol{b}} = \boldsymbol{M}^{-1}\left(\boldsymbol{M}\boldsymbol{v_b} \times \boldsymbol{\omega_b} + m_0 g \boldsymbol{R}^{\boldsymbol{T}}\boldsymbol{k} + \boldsymbol{F}_{\text{ext}}\right) \tag{2}$$

$$\dot{\boldsymbol{\omega}}_{\boldsymbol{b}} = \boldsymbol{I}^{-1}\left(-\dot{\boldsymbol{I}}\boldsymbol{\omega_b} + \boldsymbol{I}\boldsymbol{\omega_b} \times \boldsymbol{\omega_b} + \boldsymbol{M}\boldsymbol{v}_b \times \boldsymbol{v_b} + \boldsymbol{T}_{\text{ext}} + m_w g \boldsymbol{r_w} \times \left(\boldsymbol{R}^{\boldsymbol{T}}\boldsymbol{k}\right) + \bar{m} g \boldsymbol{r_p} \times \left(\boldsymbol{R}^{\boldsymbol{T}}\boldsymbol{k}\right)\right) \tag{3}$$

Here $\boldsymbol{M} = (m_s + \bar{m})\boldsymbol{I}_3 + \boldsymbol{M_f}$, where $\boldsymbol{I}_3$ is the 3×3 identity matrix, and $\boldsymbol{M_f}$ is the added-mass matrix, which can be calculated

via strip theory [31]. $\boldsymbol{I}$ is the sum of the inertia matrix due to the stationary mass distribution and the added inertia matrix in water. In addition, $\boldsymbol{k}$ is the unit vector along the Az direction in the inertial frame, $\boldsymbol{r_w}$ is a constant vector, and $\boldsymbol{r_p}$ is the controllable movable mass position vector, which has one degree of freedom in the Ox_b direction, $\boldsymbol{r_p} = (r_p \quad 0 \quad 0)^T$. $\boldsymbol{F}_{\text{ext}}$ stands for all external forces: the external thrust force $\boldsymbol{F_t}$ induced by tail flapping, and the external hydrodynamic forces (lift force, drag force, and side force) acting on the gliding robotic fish body, expressed in the body-fixed frame. Finally, $\boldsymbol{T}_{\text{ext}}$ is the total hydrodynamic moment caused by $\boldsymbol{F}_{\text{ext}}$.

2.2 Hydrodynamic Model. In order to model the hydrodynamics, we first introduce the velocity reference frame $Ox_vy_vz_v$. Ox_v axis is along the direction of the velocity, and Oz_v lies in the sagittal plane perpendicular to Ox_v. Rotation matrix $\boldsymbol{R}_{bv}$ represents the rotation operation from the velocity reference frame to the body-fixed frame

$$\boldsymbol{R}_{bv} = \begin{pmatrix} \cos\alpha\cos\beta & -\cos\alpha\sin\beta & -\sin\alpha \\ \sin\beta & \cos\beta & 0 \\ \sin\alpha\cos\beta & -\sin\alpha\sin\beta & \cos\alpha \end{pmatrix} \tag{4}$$

where the angle of attack $\alpha = \arctan(v_3/v_1)$ and the sideslip angle $\beta = \arcsin(v_2/||\boldsymbol{v_b}||)$.

The hydrodynamic forces include the lift force L, the drag force D, and the side force F_S; the hydrodynamic moments include the roll moment M_1, the pitch moment M_2, and the yaw moment M_3. All of those forces and moments are defined in the velocity frame [32]. And if we further assume that the tail is not flapping, which means $\boldsymbol{F_t} = 0$, we will have the following relationship:

$$\boldsymbol{F}_{\text{ext}} = \boldsymbol{R}_{bv}(-D \quad F_S \quad -L)^T \tag{5}$$

$$\boldsymbol{T}_{\text{ext}} = \boldsymbol{R}_{bv}(M_1 \quad M_2 \quad M_3)^T \tag{6}$$

The hydrodynamic forces and moments are dependent on the angle of attack α, the sideslip angle β, the velocity magnitude V [30,33], and the tail angle δ

$$D = 1/2\rho V^2 S(C_{D0} + C_D^\alpha \alpha^2 + C_D^\delta \delta^2) \tag{7}$$

$$F_S = 1/2\rho V^2 S(C_{F_S}^\beta \beta + C_{F_S}^\delta \delta) \tag{8}$$

$$L = 1/2\rho V^2 S(C_{L0} + C_L^\alpha \alpha) \tag{9}$$

$$M_1 = 1/2\rho V^2 S(C_{M_R}^\beta \beta + K_{q1}\omega_1) \tag{10}$$

$$M_2 = 1/2\rho V^2 S(C_{M_0} + C_{M_P}^\alpha \alpha + K_{q2}\omega_2) \tag{11}$$

$$M_3 = 1/2\rho V^2 S(C_{M_Y}^\beta \beta + K_{q3}\omega_3 + C_{M_Y}^\delta \delta) \tag{12}$$

where ρ is the density of water and S is the frontal cross-sectional area of the gliding robotic fish, defined as the characteristic area of the robot. The tail angle δ is defined as the angle between the longitudinal axis Ox_b and the center line of the tail projected into the Ox_by_b plane, with Oz_b axis as the positive direction. K_{q1}, K_{q2}, K_{q3} are rotation damping coefficients. All other constants with "C" in their notations are hydrodynamic coefficients, whose values can be evaluated through computational fluid dynamics (CFD)-based water tunnel simulation [29,34].

3 Three-Dimensional Spiraling Motion of the Gliding Robotic Fish

We have three control variables available to manipulate the locomotion profile of the gliding robotic fish: excess mass m_0, the position of the movable mass $\boldsymbol{r_p}$, and the tail angle δ. In this section, we derive the steady-state spiraling equations with three control inputs fixed and the use of Newton's method to solve the equations recursively, followed by numerical exploration of the region of convergence for the method. Then, local stability is checked through linearization, and the basins of attraction are studied through the simulation of full dynamics.

3.1 Steady-State Spiraling Equations. If control inputs are fixed with a nonzero tail angle, we can treat the influence of the tail on the hydrodynamic forces and moments as the effects of increased hydrodynamic angles (α, β). The robot will perform three-dimensional spiraling motion, where the yaw angle ψ changes at constant rate while the roll angle ϕ and pitch angle θ are constants at the steady state. Then, $\boldsymbol{R^T k}$ is constant since

$$\boldsymbol{R^T k} = \boldsymbol{R^T}\begin{pmatrix} 0 \\ 0 \\ 1 \end{pmatrix} = \begin{pmatrix} -\sin\theta \\ \sin\phi\cos\theta \\ \cos\phi\cos\theta \end{pmatrix} \tag{13}$$

Take time derivative of $\boldsymbol{R^T k}$, we have

$$\boldsymbol{\omega_b} \times (\boldsymbol{R^T k}) = 0 \tag{14}$$

so the angular velocity has only one degree of freedom with an amplitude of ω_{3i} in the Oz direction in the inertial frame. Then

$$\boldsymbol{\omega}_b = \omega_{3i}(\boldsymbol{R^T k}) \tag{15}$$

The translational velocity of the robot expressed in the body-fixed frame

$$\boldsymbol{v_b} = \boldsymbol{R}_{bv}(V \quad 0 \quad 0)^T \tag{16}$$

There are two important parameters in the spiraling motion: the turning radius R and the vertical speed V_{vertical}. By projecting the robot trajectory onto the horizontal plane and the velocity into the vertical direction, we have the following approximations for the turning radius and the vertical speed

$$R = V\cos(\theta - \alpha)/\omega_{3i} \tag{17}$$

$$V_{\text{vertical}} = V\sin(\theta - \alpha) \tag{18}$$

The steady-state spiraling equations are obtained by setting time derivatives to zero in Eqs. (2) and (3)

$$0 = \boldsymbol{M v_b} \times \boldsymbol{\omega_b} + m_0 g \boldsymbol{R^T k} + \boldsymbol{F}_{\text{ext}} \tag{19}$$

$$0 = \boldsymbol{I\omega_b} \times \boldsymbol{\omega_b} + \boldsymbol{M v}_b \times \boldsymbol{v_b} + \boldsymbol{T}_{\text{ext}} + m_w g \boldsymbol{r_w} \times (\boldsymbol{R^T k}) + \bar{m} g \boldsymbol{r_p} \times (\boldsymbol{R^T k}) \tag{20}$$

From Eqs. (1), (4), (15), (16), and the above steady-state spiraling equations, we know that there are six independent states for describing the steady spiral motion: $(\theta \ \phi \ \omega_{3i} \ V \ \alpha \ \beta)$ with $(m_0 \ r_p \ \delta)$ as the three control inputs. Expanding Eqs. (2) and (3), and then transforming the original states to the above six independent states, we can obtain the nonlinear steady-state spiraling equations as in the equations below:

$$\begin{aligned} 0 = {} & m_2 \sin\beta V\cos\phi\cos\theta\omega_{3i} - m_3\sin\alpha\cos\beta V\sin\phi\cos\theta\omega_{3i} \\ & - m_0 g\sin\theta + 1/2\rho V^2 S(C_{L0} + C_L^\alpha\alpha)\sin\alpha \\ & - 1/2\rho V^2 S(C_{F_S}^\beta\beta + C_{F_S}^\delta\delta)\cos\alpha\sin\beta \\ & - 1/2\rho V^2 S(C_{D0} + C_D^\alpha\alpha^2 + C_D^\delta\delta^2)\cos\alpha\cos\beta \end{aligned} \tag{21}$$

$$\begin{aligned} 0 = {} & -m_3\sin\alpha\cos\beta V\sin\theta\omega_{3i} - m_1\cos\alpha\cos\beta V\cos\phi\cos\theta\omega_{3i} \\ & - 1/2\rho V^2 S(C_{D0} + C_D^\alpha\alpha^2 + C_D^\delta\delta^2)\sin\beta \\ & + 1/2\rho V^2 S(C_{F_S}^\beta\beta + C_{F_S}^\delta\delta)\cos\beta + m_0 g\sin\phi\cos\theta \end{aligned} \tag{22}$$

$$0 = m_1 \cos\alpha\cos\beta V \sin\phi\cos\theta\omega_{3i} + m_2 \sin\beta V \sin\theta\omega_{3i} - 1/2\rho V^2 S(C_{D0} + C_D^\alpha \alpha^2 + C_D^\delta \delta^2)\sin\alpha\cos\beta - 1/2\rho V^2 S(C_{F_S}^\beta \beta + C_{F_S}^\delta \delta)\sin\alpha\sin\beta - 1/2\rho V^2 S(C_{L0} + C_L^\alpha \alpha)\cos\alpha + m_0 g\cos\phi\cos\theta \quad (23)$$

$$0 = (I_2 - I_3)\sin\phi\cos\theta\cos\phi\cos\theta\omega_{3i}^2 + (m_2 - m_3)\sin\beta\sin\alpha\cos\beta V^2 - m_w g r_w \sin\phi\cos\theta - 1/2\rho V^2 S(C_{M_0} + C_{M_P}^\alpha \alpha + K_{q2}\sin\phi\cos\theta\omega_{3i})\cos\alpha\sin\beta + 1/2\rho V^2 S(C_{M_R}^\beta \beta - K_{q1}\sin\theta\omega_{3i})\cos\alpha\cos\beta - 1/2\rho V^2 S(C_{M_Y}^\beta \beta + K_{q3}\cos\phi\cos\theta\omega_{3i} + C_{M_Y}^\delta \delta)\sin\alpha \quad (24)$$

$$0 = (I_1 - I_3)\sin\theta\cos\phi\cos\theta\omega_{3i}^2 + (m_3 - m_1)\cos\alpha\cos\beta\sin\alpha\cos\beta V^2 - m_w g r_w \sin\theta - \bar{m} g r_p \cos\phi\cos\theta + 1/2\rho V^2 S(C_{M_R}^\beta \beta - K_{q1}\sin\theta\omega_{3i})\sin\beta + 1/2\rho V^2 S(C_{M_0} + C_{M_P}^\alpha \alpha + K_{q2}\sin\phi\cos\theta\omega_{3i})\cos\beta \quad (25)$$

$$0 = (I_2 - I_1)\sin\theta\sin\phi\cos\theta\omega_{3i}^2 + (m_1 - m_2)\cos\alpha\cos\beta\sin\beta V^2 + \bar{m} g r_p \sin\phi\cos\theta - 1/2\rho V^2 S(C_{M_0} + C_{M_P}^\alpha \alpha + K_{q2}\sin\phi\cos\theta\omega_{3i})\sin\alpha\sin\beta + 1/2\rho V^2 S(C_{M_R}^\beta \beta - K_{q1}\sin\theta\omega_{3i})\sin\alpha\cos\beta + 1/2\rho V^2 S(C_{M_Y}^\beta \beta + K_{q3}\cos\phi\cos\theta\omega_{3i} + C_{M_Y}^\delta \delta)\cos\alpha \quad (26)$$

Here, we assume that the mass matrix and the inertia matrix have the following form:

$$\boldsymbol{M} = \begin{pmatrix} m_1 & 0 & 0 \\ 0 & m_2 & 0 \\ 0 & 0 & m_3 \end{pmatrix} \qquad \boldsymbol{I} = \begin{pmatrix} I_1 & 0 & 0 \\ 0 & I_2 & 0 \\ 0 & 0 & I_3 \end{pmatrix}$$

3.2 Newton's Method for Solving the Nonlinear Steady-State Spiraling Equations. The steady-state spiraling equations are highly nonlinear due to the terms involving trigonometric functions and inverse trigonometric functions. Given the angle of attack α, the sideslip angle β, and the velocity magnitude V, a recursive algorithm based on fixed-point iteration could potentially be applied to solve the equations for the other system states and control inputs [24]. However, we are more interested in the converse problem of how to calculate steady-state solutions given fixed control inputs, which are more useful for path planning and control purposes. Unfortunately, this problem does not admit analytical solutions and the convergence condition for the corresponding fixed-point problem is not satisfied. In the following, we apply Newton's method to solve the problem.

Let $\boldsymbol{x} = (\theta\ \phi\ \omega_{3i}\ V\ \alpha\ \beta)^T$ be the six states that we want to solve for steady-state spiral gliding equations. And let $\boldsymbol{u} = (m_0\ r_p\ \delta)^T$ be the three control inputs. For convenience of presentation, we write the governing equations in a compact form

$$0 = \boldsymbol{f}(\boldsymbol{x}, \boldsymbol{u}) = (f_i(\boldsymbol{x}, \boldsymbol{u}))_{i=1,\ldots,6} \quad (27)$$

For example, f_1 is the right-hand side of Eq. (21).

The iterative algorithm for Newton's method reads [35]

$$\hat{\boldsymbol{x}}_{i+1} = \hat{\boldsymbol{x}}_i - J^{-1}(\hat{\boldsymbol{x}}_i, \boldsymbol{u})\boldsymbol{f}(\hat{\boldsymbol{x}}_i, \boldsymbol{u}) \quad (28)$$

Here $\hat{\boldsymbol{x}}_i$ is the ith-step iteration for the steady states, and $J(\boldsymbol{x}, \boldsymbol{u})$ is the Jacobian matrix of $f(\boldsymbol{x}, \boldsymbol{u})$

$$J(\boldsymbol{x}, \boldsymbol{u}) = \frac{\partial \boldsymbol{f}}{\partial \boldsymbol{x}} = \left(\frac{\partial f_i}{\partial x_j}\right)_{6\times 6} \quad (29)$$

The first-row elements of the Jacobian matrix are given in Eqs. (30)–(35), while the other elements, which can be calculated analogously, are omitted in the interest of succinct presentation.

$$\partial f_1/\partial x_1 = -m_2 \sin\beta V \cos\phi \sin\theta\omega_{3i} + m_3 \sin\alpha\cos\beta V \sin\phi\sin\theta\omega_{3i} - m_0 g\cos\theta \quad (30)$$

$$\partial f_1/\partial x_2 = -m_2 \sin\beta V \sin\phi\cos\theta\omega_{3i} - m_3 \sin\alpha\cos\beta V\cos\phi\cos\theta\omega_{3i} \quad (31)$$

$$\partial f_1/\partial x_3 = m_2 \sin\beta V\cos\phi\cos\theta - m_3 \sin\alpha\cos\beta V\sin\phi\cos\theta \quad (32)$$

$$\partial f_1/\partial x_4 = m_2 \sin\beta\cos\phi\cos\theta\omega_{3i} - m_3 \sin\alpha\cos\beta\sin\phi\cos\theta\omega_{3i} - \rho VS(C_{D0} + C_D^\alpha\alpha^2 + C_D^\delta\delta^2)\cos\alpha\cos\beta - \rho VS(C_{F_S}^\beta\beta + C_{F_S}^\delta\delta)\cos\alpha\sin\beta + \rho VS(C_{L0} + C_L^\alpha\alpha)\sin\alpha \quad (33)$$

$$\partial f_1/\partial x_5 = -m_3\cos\alpha\cos\beta V\sin\phi\cos\theta\omega_{3i} - \rho V^2 SC_D^\alpha\alpha\cos\alpha\cos\beta + 1/2\rho V^2 S(C_{D0} + C_D^\alpha\alpha^2 + C_D^\delta\delta^2)\sin\alpha\cos\beta + 1/2\rho V^2 S(C_{F_S}^\beta\beta + C_{F_S}^\delta\delta)\sin\alpha\sin\beta + 1/2\rho V^2 SC_L^\alpha\sin\alpha + 1/2\rho V^2 S(C_{L0} + C_L^\alpha\alpha)\cos\alpha \quad (34)$$

$$\partial f_1/\partial x_6 = m_2\cos\beta V\cos\phi\cos\theta\omega_{3i} + m_3\sin\alpha\sin\beta V\sin\phi\cos\theta\omega_{3i} + 1/2\rho V^2 S(C_{D0} + C_D^\alpha\alpha^2 + C_D^\delta\delta^2)\cos\alpha\sin\beta - 1/2\rho V^2 SC_{F_S}^\beta\cos\alpha\sin\beta - 1/2\rho V^2 S(C_{F_S}^\beta\beta + C_{F_S}^\delta\delta)\cos\alpha\cos\beta \quad (35)$$

To emulate the gliding and spiraling motions of a gliding robotic fish, in this paper we consider a fish-shaped miniature underwater glider [29] with a swappable tail. This lab-developed robot changes its net buoyancy by pumping water in and out of an interior tank and varies its center of gravity via moving the battery pack using a linear actuator. Tails with different bending angles can be easily set up for the spiraling experiments. The prototype weighs 4.2 kg in total including a 0.8 kg movable battery pack and measures 50 cm long. Hydrodynamic coefficients are determined by CFD simulation as in Ref. [29]. Here, we want to add that the hydrodynamic coefficients regarding the tail are obtained by curve

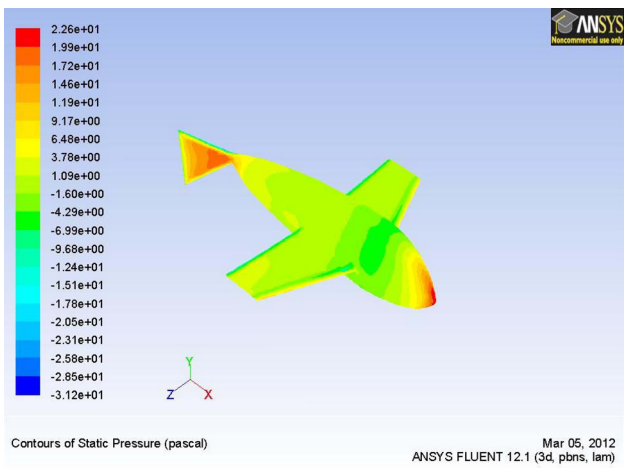

Fig. 3 Contours of the static pressure with tail angle at 45 deg

Table 1 Parameters of the lab-developed underwater robot used in the steady-state spiraling equations

Parameter	Value	Parameter	Value
m_1	3.88 kg	m_2	9.9 kg
m_3	5.32 kg	$\bar{m}$	0.8 kg
C_{D0}	0.45	C_D^{α}	17.59 rad^{-2}
$C_{F_S}^{\beta}$	−2 rad^{-1}	$C_{F_S}^{\delta}$	1.5 rad^{-1}
C_{L0}	0.075	C_L^{α}	19.58 rad^{-1}
I_1	0.8 kg·m^2	I_2	0.05 kg·m^2
I_3	0.08 kg·m^2	C_{M_0}	0.0076 m
$C_{M_R}^{\beta}$	−0.3 m/rad	$C_{M_P}^{\alpha}$	0.57 m/rad
$C_{M_Y}^{\beta}$	5 m/rad	$C_{M_Y}^{\delta}$	−0.2 m/rad
K_{q1}	−0.1 m·s/rad	K_{q2}	−0.5 m·s/rad
K_{q3}	−0.1 m·s/rad	S	0.012 m^2

fitting of the coefficients at different tail angles, which are evaluated by simulating the flow and pressure distribution using FLUENT6.2.16 in the CFD-based water channel experiments (Fig. 3).

Based on the parameters of this prototype as listed in Table 1, Newton's iterative formula is used to solve the steady-state spiraling equations. Characteristic parameters for steady spiraling motion, including the turning radius and ascending/descending speed, are obtained with different inputs as shown in Table 2. To apply Newton's method, the initial values of states for iteration are chosen to be $\theta = -10\,\text{deg}, \phi = -10\,\text{deg}, \omega_{3i} = 0.1$ rad/s, $V = 0.3\,\text{m/s}, \alpha = 0\,\text{deg}, \beta = 0\,\text{deg}$. From the calculated results, we can see that a small turning radius requires a large tail angle, a large displacement of movable mass, and a small net buoyancy, while a low descending or ascending speed demands a small tail angle, a small displacement of movable mass, and a medium net buoyancy.

3.3 Region of Convergence for Newton's Method. For Newton's method, the choice of the initial condition is important to the convergence of the algorithm. Here, we numerically explore the region of convergence. For a fixed set of control inputs, e.g., $r_p = 5\,\text{mm}, m_0 = 30\,\text{g}$, and $\delta = 30\,\text{deg}$, we carry out the convergence test by running the algorithm starting from different initial values of the states and record whether a given initial condition leads to convergence. Figure 4(*a*) shows the convergence test results for different initial conditions of the roll angle ϕ, pitch angle θ, and spiraling speed V while the initial values of the other three states are set as $\alpha = 0\,\text{deg}, \beta = 0\,\text{deg}, \omega_{3i} = 0.1\text{rad/s}$; Fig. 4(*b*) shows the results for different initial conditions of the angle of attack α, sideslip angle β, and the angular speed ω_{3i} with the initial values of the other three states set as $\phi = -10\,\text{deg}$,

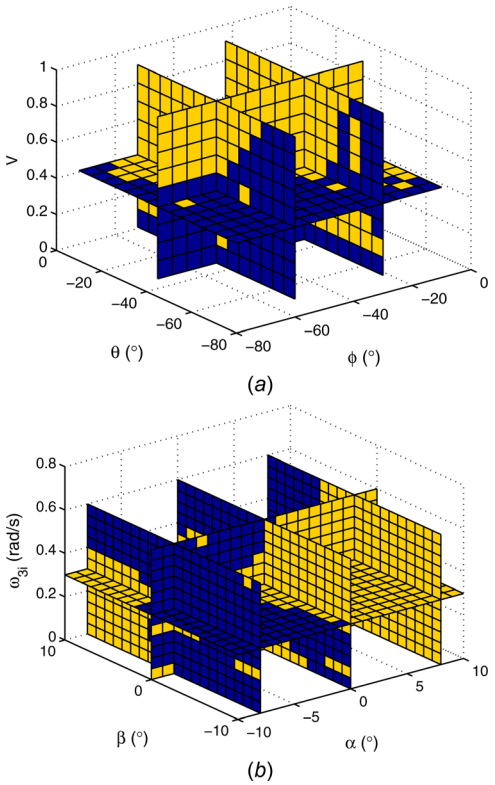

Fig. 4 Convergence test results for Newton's method with respect to initial conditions. Color yellow (light) means that convergence to the steady-state spiraling equilibrium is achievable with the corresponding initial values; color blue (dark) means that there is no convergent solution or the convergent solution is not at the steady-state spiraling equilibrium. In the test, the used set of control inputs is $r_p = 5\,\text{mm}, m_0 = 30\,\text{g}, \delta = 45\,\text{deg}$; and the corresponding equilibrium state values are $\theta = -42.1281\,\text{deg}, \phi = -34.2830\,\text{deg}, \omega_{3i} = 0.4229\,\text{rad/s}, V = 0.2809\,\text{m/s}, \alpha = -0.9014\,\text{deg}, \beta = 4.2414\,\text{deg}$. (*a*) Convergence with respect to the roll angle, pitch angle, and spiraling speed; (*b*) convergence with respect to the angle of attack, sideslip angle, and angular speed.

Table 2 Computed spiraling steady states through Newton's method

m_0 (g)	r_p (cm)	δ(deg)	$(\theta, \phi, \omega_{3i}, V, \alpha, \beta)(^\circ, ^\circ, \text{rad/s}, \text{m/s}, ^\circ, ^\circ)$	$(V_{\text{vertical}}, R)(\text{m/s}, \text{m})$
25	0.3	45	(−44.5, −31.0, 0.425, 0.264, −0.914, 4.10)	(0.182, 0.450)
25	0.4	45	(−46.8, −36.6, 0.448, 0.267, −1.32, 4.52)	(0.190, 0.417)
25	0.5	45	(−48.3, −40.6, 0.464, 0.268, −1.61, 4.87)	(0.195, 0.396)
25	0.6	45	(−49.3, −43.8, 0.476, 0.267, −1.84, 5.18)	(0.197, 0.380)
25	0.7	45	(−50.2, −46.5, 0.486, 0.267, −2.04, 5.48)	(0.211, 0.338)
10	0.5	45	(−70.8, −49.3, 0.589, 0.184, −3.64, 7.36)	(0.169, 0.121)
15	0.5	45	(−63.5, −52.7, 0.571, 0.218, −3.30, 6.98)	(0.189, 0.190)
20	0.5	45	(−55.5, −47.8, 0.517, 0.247, −2.46, 5.85)	(0.197, 0.287)
30	0.5	45	(−42.1, −34.3, 0.423, 0.281, −0.901, 4.24)	(0.185, 0.500)
35	0.5	45	(−36.9, −29.3, 0.392, 0.289, −0.306, 3.85)	(0.172, 0.591)
40	0.5	45	(−32.3, −25.3, 0.368, 0.293, 0.224, 3.60)	(0.157, 0.670)
25	0.5	30	(−37.6, −11.9, 0.235, 0.242, 0.854, 2.19)	(0.151, 0.806)
25	0.5	35	(−43.4, −20.7, 0.311, 0.258, 0.0698, 2.87)	(0.178, 0.602)
25	0.5	40	(−46.8, −31.2, 0.389, 0.266, −0.761, 3.77)	(0.192, 0.474)
25	0.5	50	(−49.2, −48.8, 0.537, 0.264, −2.54, 6.19)	(0.192, 0.337)
25	0.5	55	(−51.1, −56.4, 0.615, 0.257, −3.62, 7.86)	(0.190, 0.283)
25	0.5	60	(−55.0, −63.8, 0.705, 0.247, −4.95, 10.0)	(0.189, 0.225)

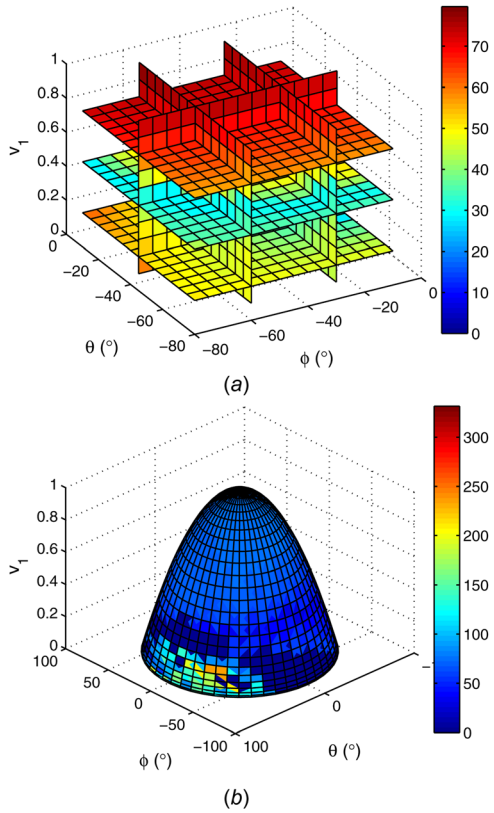

Fig. 5 Convergence time in seconds for spiraling dynamics with respect to different initial values of states in roll angle ϕ, pitch angle θ, and translational velocity v_1 along the Ox_b direction, for the control inputs of $r_p = 5$ mm, $m_0 = 30$ g, and $\delta = 45$ deg. The corresponding equilibrium state values are $\theta = -42.1281$ deg, $\phi = -34.2830$ deg, and $v_1 = 0.2801$ m/s. (*a*) Display in orthogonal slice planes and (*b*) display in a half sphere surface.

$\theta = -10\,\text{deg}, V = 0.3\,\text{m/s}$. From the results, we see that a small roll angle, a small pitch angle, and a large velocity in the reasonable range will lead to convergence; and the signs of the angle of attack and sideslip angle are very important to the convergence of the solution. These observations offer insight into how to properly choose the initial conditions when running the Newton's method to obtain the steady spiraling path; for example, one may want to

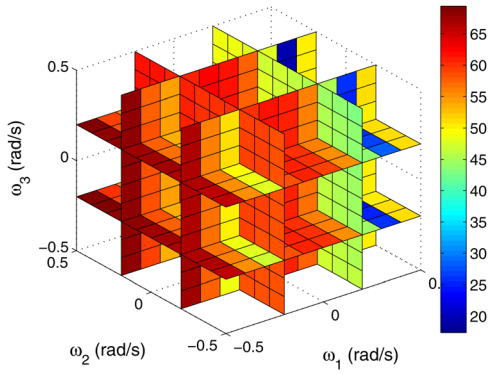

Fig. 6 Convergence time in seconds for spiraling dynamics with respect to different initial values of states in angular velocities, for the control inputs of $r_p = 5$ mm, $m_0 = 30$ g, and $\delta = 45$ deg, displayed in orthogonal slice planes. The corresponding equilibrium state values are $\omega_1 = 0.2837$ rad/s, $\omega_2 = -0.1767$ rad/s, and $\omega_3 = 0.2592$ rad/s.

select 0 deg for the initial values of the angle of attack and sideslip angle when having no idea about the signs of those two variables.

3.4 Stability Analysis of Spiraling Motion. It is of interest to understand the stability of the spiral motion under a given set of control inputs. Global stability analysis, however, is very difficult if not impossible due to the highly nonlinear dynamics of the system. In this subsection, we perform local stability analysis for the steady spiraling motion obtained from Eqs. (21)–(26). A solution to these equations can be considered a relative equilibrium of the system since it is independent of the coordinates of the robot in the inertial frame. We denote with $J_d(\boldsymbol{x_d}, \boldsymbol{u})$ the Jacobian matrix for the dynamics (2) and (3), where in a compact form the system state vector is represented as $\boldsymbol{x_d} = (\,\boldsymbol{v_b}\ \boldsymbol{\omega_b}\,)^T$ and the system dynamics as $\dot{\boldsymbol{x}}_{\boldsymbol{d}} = \boldsymbol{f_d}(\boldsymbol{x_d}, \boldsymbol{u})$. As the (relative) equilibrium point is computed using a different set of system states $\boldsymbol{x} = (\,\theta\ \phi\ \omega_{3i}\ \alpha\ \beta\,)^T$, and the Jacobian matrix $J(\boldsymbol{x}, \boldsymbol{u})$ for the steady-state equations has been evaluated with those states (Sec. 3.2), we can evaluate J_d through the chain rule

$$J_d(\boldsymbol{x_d}, \boldsymbol{u}) = \begin{pmatrix} \boldsymbol{M}^{-1} & 0 \\ 0 & \boldsymbol{I}^{-1} \end{pmatrix} J(\boldsymbol{x}, \boldsymbol{u}) \left(\frac{\mathrm{d}\boldsymbol{x_d}}{\mathrm{d}\boldsymbol{x}}\right)^{-1} \tag{36}$$

where $\dfrac{\mathrm{d}\boldsymbol{x_d}}{\mathrm{d}\boldsymbol{x}} = h(\boldsymbol{x})_{6\times 6} =$

$$\begin{pmatrix} 0 & 0 & 0 & \cos\alpha\cos\beta & -V\sin\alpha\cos\beta & -V\cos\alpha\sin\beta \\ 0 & 0 & 0 & \sin\beta & 0 & V\cos\beta \\ 0 & 0 & 0 & \sin\alpha\cos\beta & V\cos\alpha\cos\beta & -V\sin\alpha\sin\beta \\ -\cos\theta\omega_{3i} & 0 & -\sin\theta & 0 & 0 & 0 \\ -\sin\phi\sin\theta\omega_{3i} & \cos\phi\cos\theta\omega_{3i} & \sin\phi\cos\theta & 0 & 0 & 0 \\ -\cos\phi\sin\theta\omega_{3i} & -\sin\phi\cos\theta\omega_{3i} & \cos\phi\cos\theta & 0 & 0 & 0 \end{pmatrix}$$

and its determinant $|\mathrm{d}\boldsymbol{x_d}/\mathrm{d}\boldsymbol{x}| = -V^2\omega_{3i}^2\cos\beta\cos\theta$, which is not zero if the robot's translational speed V and orbiting speed ω_{3i} are not zero, and if the sideslip angle β and pitch angle θ are not $\pm\pi/2$. These conditions are satisfied for a spiraling maneuver, which implies that the inverse of matrix $\mathrm{d}\boldsymbol{x_d}/\mathrm{d}\boldsymbol{x}$ in Eq. (36) always exists.

So the value of linearization matrix J_d at the equilibrium point can be obtained by just plugging the steady-state values $\boldsymbol{x_e}$ computed in Sec. 3.2 into the above equation, and by checking the Hurwitz property of the linearization matrix J_d, we can understand the local stability property of the steady-state spiraling motion.

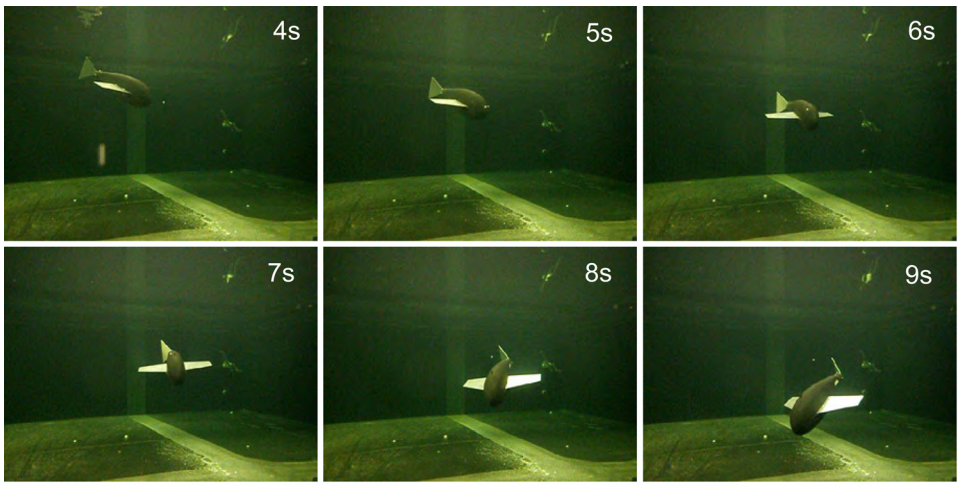

Fig. 7 Snap shots of the robot spiraling in the experiment tank. A full video of this maneuver can be accessed at[2]

We test the listed steady-state spiral motions in Table 2 for local stability. For example, for the steady spiral corresponding to the control input set $m_0 = 25\,\text{g}, r_p = 0.3\,\text{cm}$, and $\delta = 45\,\text{deg}$, the eigenvalues of Jacobian matrix J_d are $-0.91 \pm 5.02i, -6.69, -2.09, -0.42, -0.090$, which suggests stability. We find that all spirals in Table 2 have a Hurwitz Jacobian matrix and thus the equilibrium of each spiral is locally asymptotically stable.

3.5 Basins of Attraction for the Spiraling Dynamics. The analysis in the previous subsection suggests that the relative equilibria associated with steady spiraling are locally stable. It is of interest to gain some insight into the sizes of basins of attraction for those equilibria. In this subsection, we run the dynamics simulation starting from different initial conditions for a given fixed control input, and then record whether each initial state configuration will lead to convergence to steady spiraling, and if yes, what is the approximate time it takes to converge. Since one cannot visualize a state space of more than three dimensions, we have chosen to visualize the basin of attraction in three-dimensional subspaces of the original state space.

Figure 5 shows the simulation results of convergence time based on the parameters of our experimental prototype with respect to three states ϕ, θ, v_1. To obtain the results shown in this figure, the control inputs are given as $r_p = 5\,\text{mm}, m_0 = 30\,\text{g}$, and $\delta = 45\,\text{deg}$. Following this simulation method, we can get the basins of attraction with convergence time for any other set of control inputs. Similarly, we can obtain the convergence test results, shown in Fig. 6, when we vary the initial conditions for the angular velocities in the body-fixed frame. From the results, it seems that the basin of attractions for the spiraling dynamics is very large, which means that, starting from almost every state configuration in a reasonable state value range, the glider is able to achieve the steady spiraling motion eventually. However, we also notice that the convergence time varies significantly with the starting condition. When the pitch angle and roll angle are negative and the speed is neither too high nor too low, the convergence time is relatively short. This provides us with some ideas about when to switch to a desired gliding profile and how long we expect for the transient period. We also notice that among all three angular velocity states, only the initial condition of ω_1 takes a noticeable influence on the convergence time of the glider dynamics. This is consistent with the slow dynamics of the rotation motion in Ox_b direction due to the enhanced inertia from the large wings.

[2]http://www.youtube.com/watch?v=te_L2sNus4I.

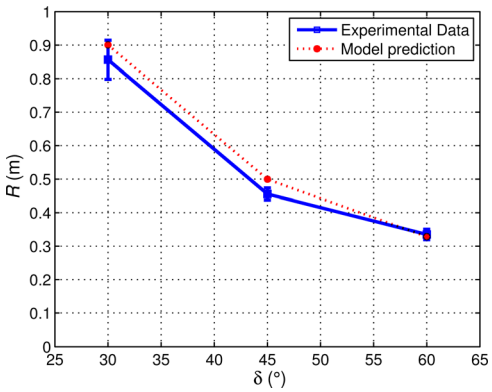

Fig. 8 Spiraling radius with respect to the tail angle, with fixed movable mass displacement of 0.5 cm and fixed excess mass of 30 g

4 Experimental Results

With the miniature underwater glider prototype featuring a swappable tail fin, experiments are conducted in order to confirm the spiraling motion and validate the derived mathematical model. The experiments are performed in a large water tank that measures 4.6 m (15 ft) long, 3.0 m (10 ft) wide, and 1.2 m (4 ft) deep, as shown in Fig. 7. We set the net buoyancy (negatively buoyant), the linear actuator position and the tail angle to fixed values. Then, the glider is released on the water surface and enters into the spiraling mode. Cameras are set to record the videos in both top view and side view. The turning radii of the spirals are extracted after video processing. The comparison between model predictions and experiment results on turning radius for different tail angles and different excess masses are shown in Figs. 8 and 9, respectively. From the results, we can see that the turning radius of the spiral is smaller with a larger deflected tail angle and a smaller net buoyancy. The error bar in the figures shows the average value and standard deviation of the turning radius out of ten repeated experiments. The model prediction shares the same trend with the experimental results, and generally speaking, the match between those two are good.

There are some factors contributing to the measurement errors. First, the scales of camera images are different at different distances. Here, an average scale is used in the information acquisition during video processing. A grid board is used for calibration, captured with the camera at the average distance. Second, there are

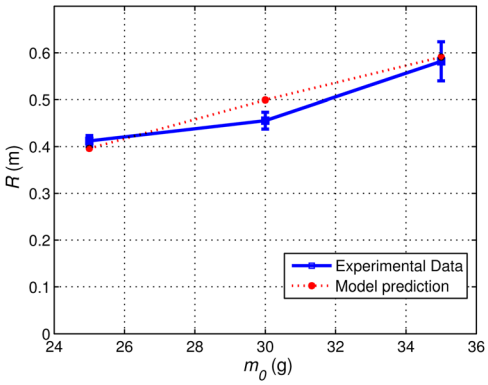

Fig. 9 Spiraling radius with respect to the excess mass, with fixed movable mass displacement of 0.5 cm and fixed tail angle of 45 deg

some initial transient processes, which is difficult to be completely separate from the steady spiraling period. Experimental environment with deeper water will effectively reduce the influence of initial transient; however, the complexity of the experimental setup will be increased as a result. The environmental disturbances such as currents will also affect the experimental results. So with these uncertainties, we consider the match between our experimental results and the model predictions satisfactory.

5 Conclusion

In this paper, we investigated a novel spiral motion for a gliding robotic fish, achieved by gliding with a deflected tail. Such spirals allow energy-efficient 3D maneuvering and thus hold strong promise in water column sampling and other mobile sensing applications. A dynamic model of gliding robotic fish was presented and the steady-state spiraling equations were derived and analyzed. Newton's method was used to solve the equations, and the stability of the resulting equilibria was analyzed. A miniature underwater glider featuring a swappable (passive) tail was used to experimentally validate the mathematical model.

The studies in this paper facilitate the future work. The presented results on the basins of attraction of the spiral motion and the convergence times at different initial conditions tell us how fast we can expect the robot to stabilize itself in the water-column sampling application, and gives insight into how to design the sampling paths and control commands in order to accommodate the limitation of the robot dynamics, in terms of response speed and motion stability.

For future work, we will first complete a full gliding robotic fish prototype that has an active tail so that one can vary the tail angle continuously in a quasi-static manner. This would allow us to study spiraling with a varying radius (for example, spiral-in and spiral-out) and thus more complex maneuvers. We will also investigate the path planning and control of gliding robotic fish for spiraling-based 3D maneuvers.

Acknowledgment

This work was supported in part by National Science Foundation (IIS 0916720, ECCS 1050236).

References

[1] Eriksen, C. C., Osse, T. J., Light, R., Wen, R. D., Lehmann, T. W., Sabin, P. L., Ballard, J. W., and Chiodi, A. M., 2001, "Seaglider: A Long-Range Autonomous Underwater Vehicle for Oceanographic Research," IEEE J. Oceanic Eng., **26**(4), pp. 424–436.
[2] Sherman, J., Davis, R. E., Owens, W. B., and Valdes, J., 2001, "The Autonomous Underwater Glider "Spray,"" IEEE J. Oceanic Eng., **26**(4), pp. 437–446.
[3] Webb, D. C., Simonetti, P. J., and Jones, C. P., 2001, "Slocum: An Underwater Glider Propelled by Environmental Energy," IEEE J. Oceanic Eng., **26**(4), pp. 447–452.
[4] Kato, N., 2000, "Control Performance in the Horizontal Plane of a Fish Robot With Mechanical Pectoral Fins," IEEE J. Oceanic Eng., **25**(1), pp. 121–129.
[5] Low, K. H., 2006, "Locomotion and Depth Control of Robotic Fish With Modular Undulating Fins," Int. J. Autom. Comput., **4**, pp. 348–357.
[6] Triantafyllou, M. S., and Triantafyllou, G. S., 1995, "An Efficient Swimming Machine," Sci. Am., **273**(3), pp. 64–70.
[7] Yu, J., and Wang, L., 2005, "Parameter Optimization of Simplified Propulsive Model for Biomimetic Robot Fish," Proceedings of the 2005 IEEE International Conference on Robotics and Automation, pp. 3306–3311.
[8] Hu, H., Liu, J., Dukes, I., and Francis, G., 2006, "Design of 3D Swim Patterns for Autonomous Robotic Fish," Proceedings of the 2006 IEEE/RSJ International Conference on Intelligent Robots and Systems, pp. 2406–2411.
[9] Morgansen, K. A., Triplett, B. I., and Klein, D. J., 2007, "Geometric Methods for Modeling and Control of Free-Swimming Fin-Actuated Underwater Vehicles," IEEE Trans. Rob., **23**(6), pp. 1184–1199.
[10] Chen, Z., Shatara, S., and Tan, X., 2010, "Modeling of Biomimetic Robotic Fish Propelled by an Ionic Polymer-Metal Composite Caudal Fin," IEEE/ASME Trans. Mechatronics, **15**(3), pp. 448–459.
[11] Anderson, J., and Chhabra, N., 2002, "Maneuvering and Stability Performance of a Robotic Tuna," Integr. Comp. Biol., **42**(1), pp. 118–126.
[12] Yu, J., Tan, M., Wang, S., and Chen, E., 2004, "Development of a Biomimetic Robotic Fish and Its Control Algorithm," IEEE Trans. Syst., Man, Cybern., Part B, **34**(4), pp. 1798–1810.
[13] Epstein, M., Colgate, J., and MacIver, M., 2006, "Generating Thrust With a Biologically-Inspired Robotic Ribbon Fin," IEEE/RSJ International Conference on Intelligent Robots and Systems, pp. 2412–2417.
[14] Kodati, P., Hinkle, J., Winn, A., and Deng, X., 2008, "Microautonomous Robotic Ostraciiform (Marco): Hydrodynamics, Design, and Fabrication," IEEE Trans. Rob., **24**(1), pp. 105–117.
[15] McIsaac, K., and Ostrowski, J., 2003, "Motion Planning for Anguilliform Locomotion," IEEE Trans. Rob. Autom., **19**(4), pp. 637–652.
[16] Saimek, S., and Li, P., 2004, "Motion Planning and Control of a Swimming Machine," Int. J. Robo. Res., **23**(1), pp. 27–53.
[17] Kelly, S., 1998, "The Mechanics and Control of Robotic Locomotion With Applications to Aquatic Vehicles," Ph.D. thesis, California Institute of Technology, Pasadena, CA.
[18] Tan, X., 2011, "Autonomous Robotic Fish as Mobile Sensor Platforms: Challenges and Potential Solutions," Marine Technol. Soc. J., **45**(4), pp. 31–40.
[19] Graver, J. G., 2005, "Underwater Gliders: Dynamics, Control, and Design," Ph.D. thesis, Princeton University, Princeton, NJ.
[20] Bhatta, P., 2006, "Nonlinear Stability and Control of Gliding Vehicles," Ph.D. thesis, Princeton University, Princeton, NJ.
[21] Mahmoudian, N., 2009, "Efficient Motion Planning and Control for Underwater Gliders," Ph.D. thesis, Virginia Polytechnic Institute and State University, Blacksburg, VA.
[22] Mahmoudian, N., Geisbert, J., and Woolsey, C., 2010, "Approximate Analytical Turning Conditions for Underwater Gliders: Implications for Motion Control and Path Planning," IEEE J. Oceanic Eng., **35**(1), pp. 131–143.
[23] Zhang, S., Yu, J., Zhang, A., and Zhang, F., 2011, "Steady Three Dimensional Gliding Motion of an Underwater Glider," IEEE International Conference on Robotics and Automation (ICRA), pp. 2392–2397.
[24] Zhang, S., Yu, J., Zhang, A., and Zhang, F., 2013, "Spiraling Motion of Underwater Gliders: Modeling, Analysis, and Experimental Results," Ocean Eng., **60**, pp. 1–13.
[25] Zhang, F., Zhang, F., and Tan, X., 2012, "Steady Spiraling Motion of Gliding Robotic Fish," IEEE/RSJ International Conference on Intelligent Robots and Systems (IROS), pp. 1754–1759.
[26] Schwartz, M., 2005, *Encyclopedia of Coastal Science*, Vol. 24, Kluwer Academic Publishers, Norwell, MA.
[27] Leonard, N. E., and Graver, J. G., 2001, "Model-Based Feedback Control of Autonomous Underwater Gliders," IEEE J. Oceanic Eng., **26**(4), pp. 633–645.
[28] Bhatta, P., and Leonard, N., 2008, "Nonlinear Gliding Stability and Control for Vehicles With Hydrodynamic Forcing," Automatica, **44**(5), pp. 1240–1250.
[29] Zhang, F., Thon, J., Thon, C., and Tan, X., 2012, "Miniature Underwater Glider: Design, Modeling, and Experimental Results," Proceedings of the 2012 IEEE International Conference on Robotics and Automation, pp. 4904–4910.
[30] Greenwood, D. T., 1988, *Principles of Dynamics*, Prentice Hall, Englewood Cliffs, NJ.
[31] Milgram, J., 2007, "Strip Theory for Underwater Vehicles in Water of Finite Depth," J. Eng. Math., **58**(1), pp. 31–50.
[32] Panton, R. L., 2005, *Incompressible Flow*, Wiley, New York.
[33] Anderson, J. D., 1998, *Aircraft Performance and Design*, McGraw-Hill, New York.
[34] Seo, D., Jo, G., and Choi, H., 2008, "Pitching Control Simulations of an Underwater Glider Using CFD Analysis," OCEANS 2008-MTS/IEEE Kobe Techno-Ocean, pp. 1–5.
[35] Kelley, C., 2003, *Solving Nonlinear Equations With Newton's Method*, Society for Industrial Mathematics, Philadelphia, PA.